


Article

# Fe–Ni/MWCNTs Nano-Composites for Hexavalent Chromium Reduction in Aqueous Environment

Zeyu Kang <sup>1</sup>, Hui Gao <sup>2,\*</sup>, Xiaolong Ma <sup>1</sup>, Xiaodong Jia <sup>1</sup>  and Dongsheng Wen <sup>1,3,\*</sup><sup>1</sup> School of Chemical and Process Engineering, University of Leeds, Leeds LS2 9JT, UK<sup>2</sup> School of Aeronautic Science and Engineering, Beihang University, Beijing 100191, China<sup>3</sup> School of Engineering and Design, Technische Universität München, 85747 Garching, Germany

\* Correspondence: h.gao@buaa.edu.cn (H.G.); d.wen@tum.de (D.W.)

**Abstract:** A novel Cr (VI) removal material was designed and produced comprising multi-walled carbon nanotubes (MWCNTs) as a support with a high specific surface area and the loaded Fe–Ni bimetallic particles as catalytic reducing agents. Such a design permits the composite particle to perform the adsorption, reduction, and immobilisation of Cr (VI) quickly and efficiently. Due to MWCNTs' physical adsorption, Cr (VI) in solution aggregates in the vicinity of the composite, and Fe rapidly reduces Cr (VI) to Cr (III) catalysed by Ni. The results demonstrated that the Fe–Ni/MWCNTs exhibits an adsorption capacity of 207 mg/g at pH = 6.4 for Cr (VI) and 256 mg/g at pH 4.8, which is about twice those reported for other materials under similar conditions. The formed Cr (III) is solidified to the surface by MWCNTs and remains stable for several months without secondary contamination. The reusability of the composites was proven by retaining at least 90% of the adsorption capacity for five instances of reutilization. Considering the facile synthesis process, low cost of raw material, and reusability of the formed Fe–Ni/MWCNTs, this work shows great potential for industrialisation.

**Keywords:** environment remediation; hexavalent chromium; catalytic reduction; multi-walled carbon nanotube; kinetics modelling



**Citation:** Kang, Z.; Gao, H.; Ma, X.; Jia, X.; Wen, D. Fe–Ni/MWCNTs Nano-Composites for Hexavalent Chromium Reduction in Aqueous Environment. *Molecules* **2023**, *28*, 4412. <https://doi.org/10.3390/molecules28114412>

Academic Editors: Guohui Dong, Na Chen, Wei Liu and Jingtao Bi

Received: 27 April 2023

Revised: 26 May 2023

Accepted: 27 May 2023

Published: 29 May 2023



**Copyright:** © 2023 by the authors. Licensee MDPI, Basel, Switzerland. This article is an open access article distributed under the terms and conditions of the Creative Commons Attribution (CC BY) license (<https://creativecommons.org/licenses/by/4.0/>).

## 1. Introduction

With the fast rise and development of human industry, waste gas, water, and solid pollution are becoming more severe, which poses a serious threat to human health [1,2]. Among them, heavy metal contamination has garnered significant attention from environmental experts and a huge amount of research has been conducted in recent years due to heavy metal bioaccumulation and non-degradability [3,4]. Chromium (Cr) is a typical heavy metal pollutant that is pervasive in the environment as a result of its broad usage in metallurgical, chemical, refractory, and cast-iron processes [5]. The predominant stable forms of chromium are trivalent chromium (Cr (III)) and hexavalent chromium (Cr (VI)). Cr (III) is a necessary element for the human body, and its toxicity is moderate [6]. The toxicity of Cr (VI), however, is about one hundred times that of Cr (III) [7], posing far greater environmental and health hazards. It can enter the human circulatory system through drinking water or food-chain enrichment and have harmful effects on people [8].

To solve the chromium pollution problem, many advanced treatment technologies such as reduction, ion exchange, adsorption, membrane filtration, and electrochemical treatment have been applied for efficient Cr (VI) removal [9]. Each method has its own benefits and drawbacks; for instance, adsorption can remove both Cr (III) and Cr (VI), but its capacity is limited [10]. Ion exchange is effective and simple to implement, but it is easily affected by other ions [11]. Membrane filtration can remove Cr (VI) on a large scale, but it is an expensive process [12]. Electrochemical treatment has a rapid reaction rate but produces an enormous amount of sludge [13]. Reduction requires only a one-step

process, but it is unsuitable for drinking-water treatment [14]. Reduction and adsorption are the two most widely used methods among these. Integrating chemical reduction and adsorption together has proven to be more promising to increase Cr (VI) removal efficiency; consequently, several types of materials designed to achieve this have been widely investigated in recent years. For example, the non-toxic and cheap zero-valent iron (ZVI) has been proposed as a chemical precipitation agent to remove chromium contaminants [15–18]. Cr (VI) could be reduced by ZVI and form insoluble Cr (III) precipitates with a much lower toxicity in a neutral or alkaline environment. Previous studies have demonstrated that conventional micrometre-sized ZVI presents the ability to remove Cr (VI), but its relatively low adsorption capacity limits its application [19]. Nano zero-valent iron (NZVI) particles have a smaller particle size and a larger specific surface area than ordinary iron powders, showing a better Cr (VI) removal potential [20–22]. Although NZVI possesses great potential as a Cr removal agent, it does not work well in practical applications, mainly because of ageing [23], a lack of selectivity and directionality (e.g., reacts with nitrate and organic matter) [24], and agglomeration [25]. In addition, the separation of NZVI from the treated solution also presents a big challenge. All of these features limit the adsorption capacity and may produce secondary pollution [26]. In order to overcome the problem, researchers have tried to modify NZVI using a variety of different methods [27], such as forming polymetallic material [28] or support by an adsorbent [29].

Normally, polymetallic particles are constituted with a corrosive metal such as iron or zinc as a reductant along with a noble metal as a catalyst such as palladium (Pd) [30], copper (Cu) [31], nickel (Ni) [32], or cerium (Ce) [33]. Huang et al. [34] synthesised nickel–iron layered double hydroxide and modified the surface charge density to achieve a Cr (VI) removal capacity of 35.86 mg/g at an initial pH of 5. Li et al. [35] created a  $\text{Cd}_{0.5}\text{Zn}_{0.5}\text{S}/\text{Bi}_2\text{WO}_6$  composite, which is capable of photocatalytically reducing Cr (VI) with a reduction efficiency of up to 95.8% at pH 5. Polymetallic materials have been proven to possess a higher Cr adsorption capacity and reaction rate compared to the pure NZVI system [36].

Certain limitations, however, also need to be solved including the aggregation problem that reduces its adsorption capacity [37], the secondary pollution of reduced Cr (III) as is not immobilized [38], and the difficulty of nanoparticle collection in practical application which may increase the operating costs [39]. Besides the polymetallic materials, porous-structured materials with a high specific surface area are proposed as excellent adsorbent candidates, such as clay minerals [40], bio sorbent materials [41], and carbon-based compounds [42]. Researchers have attempted to increase the Cr (VI) adsorption capacity by combining reducing metals or their oxides with adsorbents. For example, Zhou et al. [43] loaded nano zero-valent iron (nZVI) onto biochar made from recycled peanut shell waste; the composites achieved a 99.73 mg/g of Cr (VI) adsorption capacity at pH = 7.5. Bharath et al. [44] produced peanut-shell-derived activated carbon and its  $\text{Fe}_3\text{O}_4$  nano-composite and demonstrated a maximum electrosorption capacity of 24.5 mg/g at 1.2 V.

It is believed that a better Cr removal effect should be achieved by integrating polymetallic and sorbent-supported material together. Previous studies have demonstrated that polymetallic loading increases the adsorption capacity by approximately 50% when compared to that of pure iron loading [45]. For example, Lu et al. [46] decorated an Fe–Ni bimetal on montmorillonite and obtained an adsorption capacity of about 65 mg/g at pH = 3. Zeng et al. [47] synthesized biochar-loaded Fe–Ni bimetallic particles and observed an adsorption capacity of 55.52 mg/g at pH = 3.1. Compared to natural materials, some carbon-based artificial materials such as reduced graphene oxide (RGO), graphene oxide (GO), and multi-walled carbon nanotubes (MWCNTs) are more promising because of their high surface area and purity. For example, Bharath et al. [48] synthesized a Ru– $\text{CoFe}_2\text{O}_4$ /RGO photoelectrode with a maximum Cr (VI) reduction rate of 99.9% at 30 min when exposed to visible light. Kang et al. [49] loaded an Fe–Ni bimetal on RGO and achieved 197.43 mg/g at pH = 5. As two-dimensional RGO and GO could partly encapsu-

late metal particles and prevent them from reacting with Cr (VI), resulting in a decrease in Cr (VI) adsorption capacity and a low reusability, one-dimensional carbon materials should have a better performance compared with two-dimensional carbon materials [50]. Due to the unique tubular structure of MWCNTs and their extraordinarily high specific surface area, it is a suitable material for providing physical adsorption capacity as it ensures a high number of adsorption sites. Polymetallics such as nano iron and nickel, on the other hand, are an excellent choice for providing reduction capability. Integrating the above two materials together can ensure a target material with a high physical adsorption and chemical reduction capacity for Cr (VI); therefore, this is believed to achieve a promising Cr removal property. In the removal of Cr (VI), the following synergies are expected to occur: MWCNTs aggregate Cr (VI) in solution in the vicinity of the composite by physical adsorption; meanwhile, Fe rapidly reduces Cr (VI) to Cr (III) catalysed by Ni. MWCNTs also provide part of the Cr (VI) adsorption capacity based on their own physical adsorption. The chemical reduction capacity reduces Cr (VI) to Cr (III), which is less susceptible to re-oxidation in nature, preventing secondary contamination. The chemical reduction method will provide the majority of the Cr (VI) adsorption capacity.

Hence, this work aims to synthesize Fe–Ni/MWCNTs composite particles by loading Fe–Ni bimetallic particles onto MWCNTs through a co-precipitation and physisorption method. The adsorption capacity and reutilization properties were measured and analyzed in detail. The results indicate that the formed composite shows a higher adsorption capacity under similar conditions compared to those reported in the literature. A high adsorption capacity performance was observed for reuse. Considering the merits, including the low cost of all raw materials, simple synthesis process, and good reusability, the Fe–Ni/MWCNTs composites proposed here exhibit the potential for future industrialization.

## 2. Results and Discussion

### 2.1. Particle Size, Morphology, and Elemental Analyses

#### 2.1.1. Particle Size Analysis

A centrifuge was used to separate the sediments from the liquid after adding 15 mg of the sample solution to 50 mL of deionized water under ultrasonic dispersion. The upper liquid was tested by Zetasizer, Malvern, and the results are shown in Figure 1a and Table A1. Two peaks were found in all samples. A larger size range indicates that MWCNTs have been stacked in an unordered manner. It is clearly shorter than the length of the MWCNTs (2500 nm) shown in the purchase company data, because the MWCNTs are curved rather than straight. The particles of about 50–80 nm in diameter should represent Ni and Fe (0) NPs. Figure 1b illustrates that the pHzPC values for M3 and M3R are 6.71 and 6.77, respectively, and their zeta potentials increase with decreasing pH values. At lower pH values, when the pH values are less than pHzPC points, the samples are better dispersed and stabilized, which has a positive effect on the adsorption capacity of Cr (VI). Furthermore, when the zeta potential is positive, the samples are positively charged, and the electrostatic effect enhances their attraction to the negatively charged  $\text{Cr}_2\text{O}_7^{2-}$  in solution.

#### 2.1.2. Morphology and Elemental Analyses

TEM and SEM were used to examine the morphology and structure of the Fe–Ni/MWCNTs. The results in Figure 2 illustrate M3 as an unordered stacking of MWCNTs and Fe–Ni particles, and that the Fe–Ni bimetal particles are approximately 50–80 nm and the MWCNTs are more than 1  $\mu\text{m}$  in diameter. This is consistent with DLS data. The energy-dispersive X-ray spectroscopy (EDS) results in Figure 2e illustrate the elemental composition of M3, indicating a uniform distribution of Fe, Ni, and C elements. Comparatively, Figure 2f illustrates that Cr appears after the sorption of Cr (VI), indicating that an amount of Cr element is immobilised on the surface of the sample. However, the valence state and compound structure need further characterization via other methods to confirm. The existence of O is due to metallic particles being inevitably partially oxidised, because nitrogen protection

is not used throughout the whole synthesis process. For the M3A sample, the diameter of Fe–Ni particles decreased to around 50 nm after the Cr (VI) adsorption test. This is because part of the Fe (0) is consumed by Cr (VI) during the reduction process. Figure 2d illustrates how the Fe–Ni bimetal is decorated on the surface of MWCNTs in the HRTEM image for M3A.

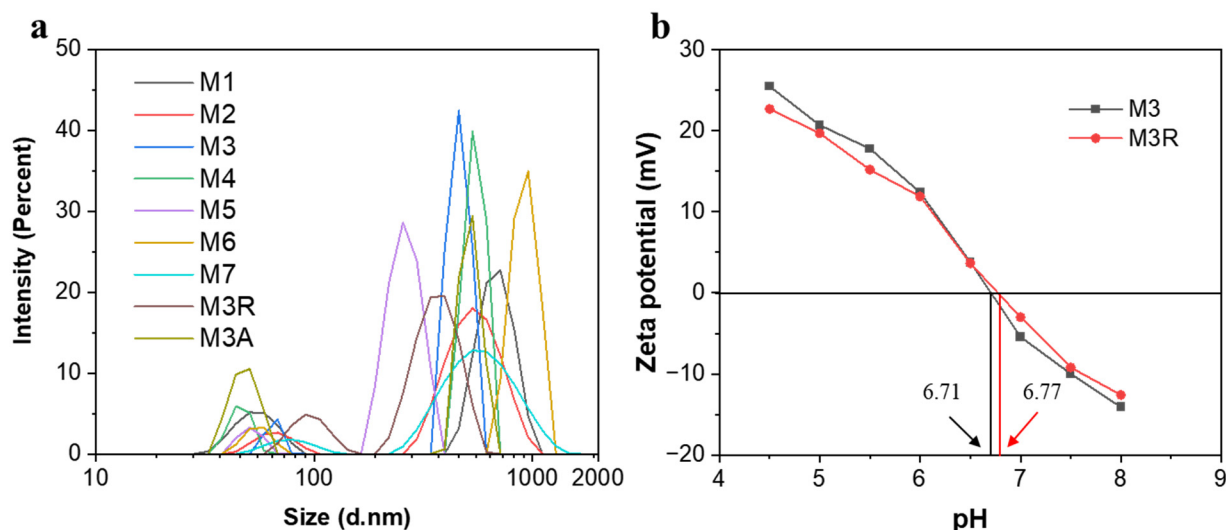


**Figure 1.** (a) Particle size distribution measured by DLS and (b) the zeta potentials of M3 and M3R at pH 4.5–8.0.

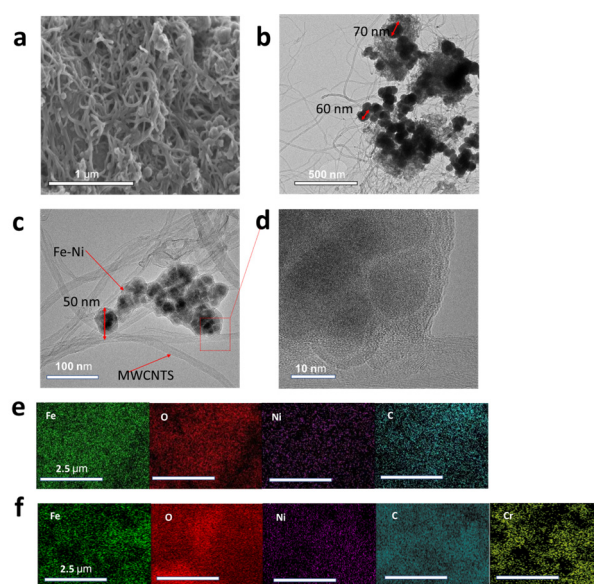


**Figure 2.** SEM image (a) and TEM image (b) for M3, TEM image (c) and HRTEM image (d) for M3A, and EDS image (e) for M3 and (f) for M3A.

Figure 3a illustrates the XRD patterns of unmodified MWCNTs, M3, and M3A. The unmodified MWCNTs exhibit a sharp peak at  $26.3^\circ$  corresponding to the typical (002) diffraction of MWCNTs (JCPDS No. 00–058–1638) [51]. Due to the covering of loaded materials, no similar sharp peaks were observed on M3 and M3A. The inevitable oxidation of Fe (0) [52] causes the double peaks at  $31.6^\circ$ ,  $35.2^\circ$ , and  $48.1^\circ$ ,  $49.2^\circ$  for M3 (JCPDS No. 01–072–6225). For M3A, the peak at  $35.1^\circ$  indicates the presence of Fe (OH)<sub>3</sub> (JCPDS No. 00–022–0346) [53], and the peaks at  $26.1^\circ$  and  $62.9^\circ$  indicate the presence of Cr (OH)<sub>3</sub> (JCPDS No. 00–012–0241) [54], both of which originate from the coordinated or adsorbed H<sub>2</sub>O in M3A. Figure 3b of the FTIR data demonstrates distinct peaks at approximately

550  $\text{cm}^{-1}$  and 1623  $\text{cm}^{-1}$ , combined with the identified elements from the EDS results, that corresponds to  $\text{Cr}(\text{OH})_3$  and  $\text{Fe}(\text{OH})_3$  coprecipitated sediment [55,56]. The lack of an obvious peak observed around 900  $\text{cm}^{-1}$  indicates that no considerable  $\text{Cr}=\text{O}$  exists [57,58]. This demonstrates that the sediment contains  $\text{Cr}(\text{III})$  and  $\text{Fe}(\text{III})$  in the form of  $\text{Cr}(\text{OH})_3$  and  $\text{Fe}(\text{OH})_3$ , respectively. It is also consistent with the XRD results. Comparing M3A and unmodified MWCNTs, the distinct peak at around 3363  $\text{cm}^{-1}$  represents the stretching and bending vibration of the  $-\text{OH}$  on MWCNTs in M3A [59]. The  $-\text{OH}$  is generated as a result of  $\text{Cr}(\text{VI})$ 's strong oxidizing ability. The absence of a prominent peak for unmodified MWCNTs and M3 suggests that there are no considerable oxygen-containing groups on MWCNTs.

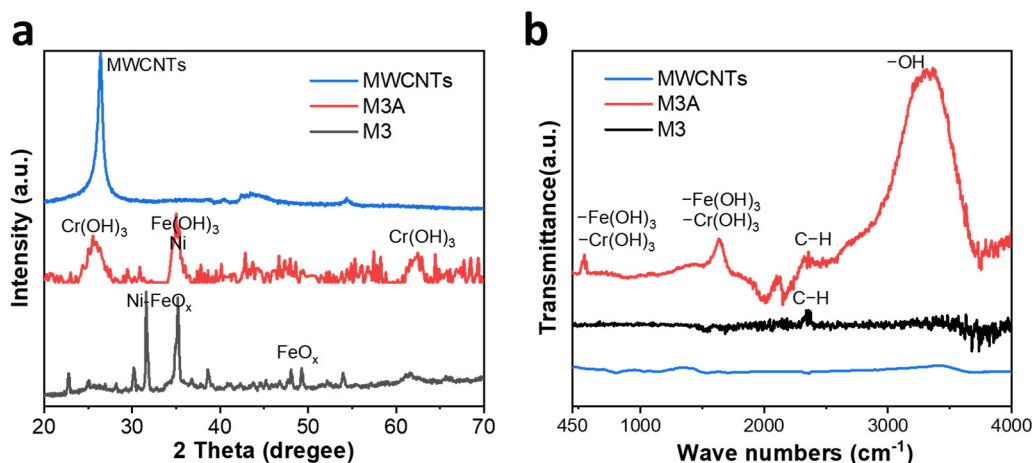


**Figure 3.** (a) XRD patterns and (b) FTIR spectra of unmodified MWCNTs, M3, and M3A.

The XPS spectra in Figure 4a confirm that the M3 and M3A samples are primarily composed of C, O, Fe, and Ni. As shown in Figure 4b, the resolution spectra of the Cr 2p region magnifies the two deconvoluted peaks of Cr 2p<sub>1/2</sub> and Cr 2p<sub>3/2</sub>. Based on the XRD and FTIR results above, the two peaks correspond to the Cr present in  $\text{Cr}(\text{III})$  [60]. It is confirmed that  $\text{Cr}(\text{VI})$  is reduced to  $\text{Cr}(\text{III})$  and adsorbed by the sample. In Figures 4c and 4d, the peaks for Fe 2p are deconvoluted into two peaks. This is due to the presence of  $\text{Fe}_2\text{O}_3$  in M3 and  $\text{Fe}(\text{OH})_3$  in M3A [61]. The binding energy for  $\text{Fe}_2\text{O}_3$  in M3 and  $\text{Fe}(\text{OH})_3$  in M3A are nearly identical [62–64]. The results from XPS are consistent with those obtained from XRD and FTIR.

## 2.2. BET Surface Area Study

The specific surface area of samples was measured by a Micromeritics Tristar 3000, as shown in Figure 5. According to the adsorption–desorption isotherm, the isotherm is a concave curve and has no inflexion point. The amount of gas adsorbed rises as the partial pressure of the components increases. The concave curve is due to the intermolecular interaction between adsorbates being stronger than that between adsorbent and adsorbates; the adsorption becomes self-accelerating as the process proceeds and exhibits multilayer adsorption characteristics [65,66]. M1, M3, and M3R have specific surface areas calculated as 23.6197  $\text{m}^2/\text{g}$ , 82.2434  $\text{m}^2/\text{g}$ , and 30.7797  $\text{m}^2/\text{g}$ , respectively. This indicates that the presence of nickel powder significantly increases the sample surface area, due to its own high surface area, and that it combines with  $\text{Fe}(0)$  to reduce the degree of Fe aggregation. In contrast, samples that contain nickel powder have a smaller distribution of pore widths. As a result of the aggregation of  $\text{Ni}(0)$  and  $\text{Fe}(0)$  during the  $\text{Cr}(\text{VI})$  adsorption experiment and the second reduction process for  $\text{Fe}(\text{III})$ , the BET surface area of M3R was much smaller than that of M3. It should be noted, however, that the BET specific surface areas of all samples were considerably lower than those of pure MWCNTs (more than 200  $\text{m}^2/\text{g}$ ). This is due to the disordered stacking of MWCNT, as indicated by the SEM results.

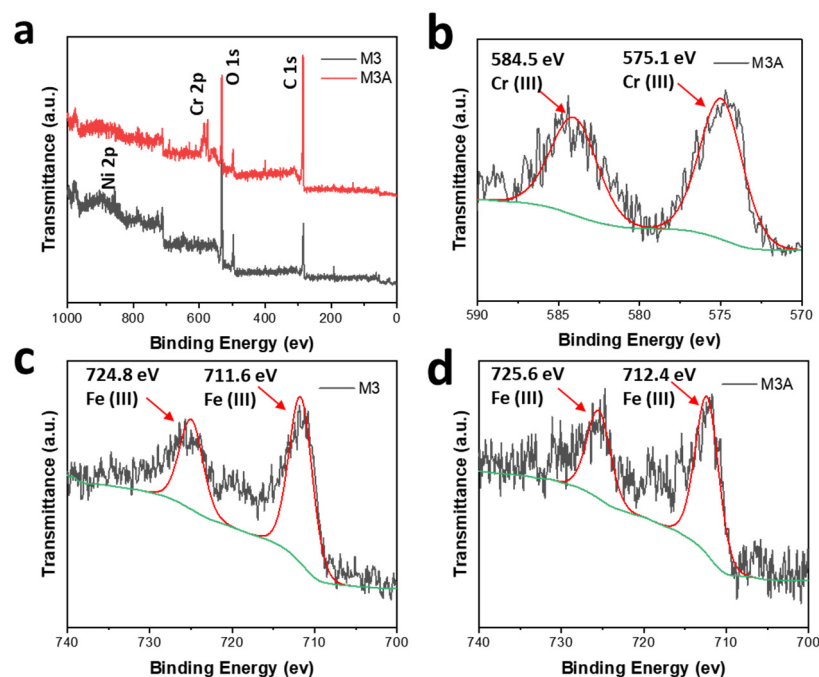


**Figure 4.** XPS spectra of M3 and M3A: (a) wide scan, (b) high resolution spectra of Cr in M3A, and high resolution spectra of Fe in (c) M3 and (d) M3A.

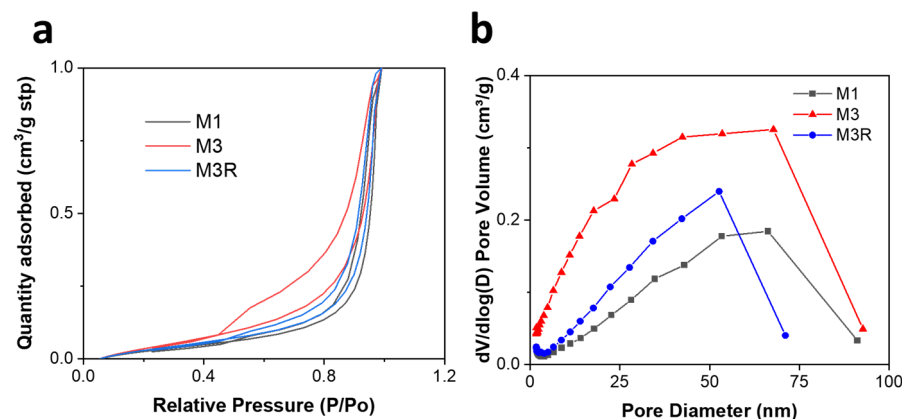


**Figure 5.** BET results of samples (a)  $N_2$  adsorption isotherms and (b) pore size distribution data.

### 2.3. Cr (VI) Adsorption Capacity Analyses

Figure 6a illustrates DPC combined with various Cr (VI) concentration solutions to produce a violet color solution with a characteristic peak at  $\lambda_{\max} = 545$  nm. A linear relationship between Cr (VI) concentration and absorbance at  $\lambda_{\max} = 545$  nm is shown in Figure 6b. In the equation  $y = 37.191x - 0.0916$  with  $R^2 = 0.9999$ ,  $x$  stands for the concentration of Cr (VI), while  $y$  stands for absorbance. Figure 6c illustrates that the Cr (VI) concentration stabilised after 20 min in most cases. Then, the adsorption capacity was calculated by analysing the remaining concentration of Cr (VI) (Table 1). Figure 6e shows the changes of strong violet color with time for Cr (VI) adsorbed by M3. The drastic diminishment of the violet indicates the decrease in Cr (VI) concentration.

Likewise, pure MWCNTs and NZVI were also tested under the same conditions for Cr (VI) adsorption capacity analyses. As shown in Table 1, pure MWCNTs and iron have very low Cr (VI) adsorption capacities. Fe (0)-decorated MWCNTs had a significantly higher adsorption capacity than pure MWCNTs and NZVI. The combined action of MWCNTs and NZVI was responsible for this result. Cr (VI) is adsorbed to the surface of MWCNTs by physical adsorption, and the adsorbed Cr (VI) is reduced by the decorated nano iron

more effectively. Comparing M1 with other samples, it is clear that the addition of a certain amount of Ni can naturally increase the Cr (VI) adsorption capacity. Due to the high catalytic performance of Ni particles, the activation energy required for the reduction of Cr (VI) is decreased. From M2 to M7, different Cr (VI) adsorption capacities are obtained due to different Fe to Ni ratios. The ideal ratio for Fe–Ni is approximately 5:1, and M3 exhibits the highest adsorption capacity at 224.43 mg/g.

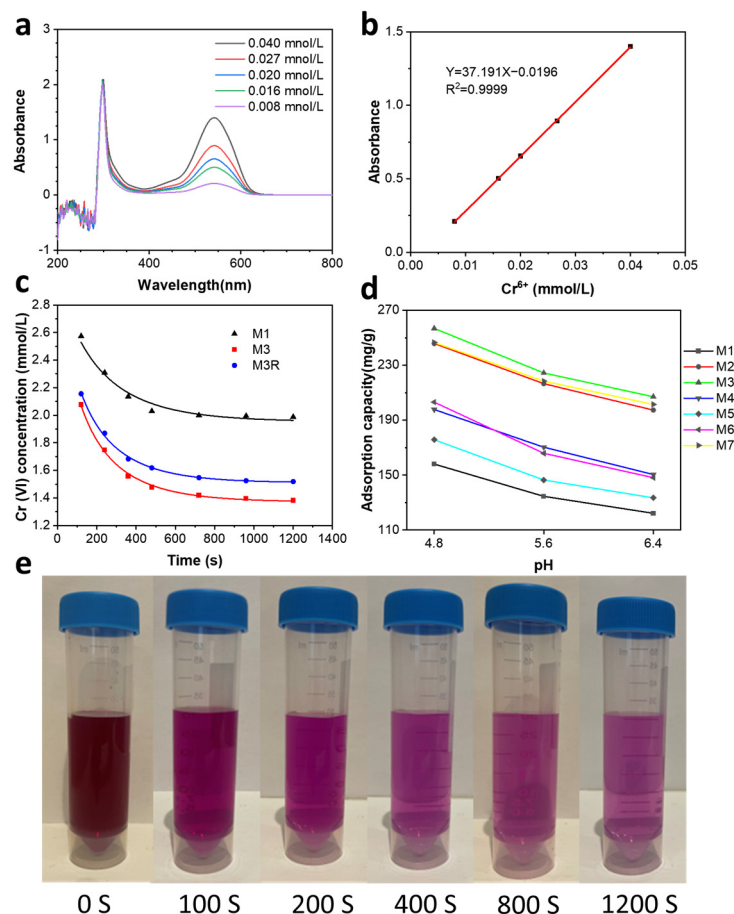


**Figure 6.** (a) UV–Vis spectra of solutions of Cr (VI) reaction with DPC; (b) calibration curve line of Cr (VI) concentration ( $\lambda = 545$  nm); (c) Cr (VI) adsorption capacity at different pH values; (d) Cr (VI) adsorption capacity with time and pseudo-second-order kinetic model; (e) Cr (VI) adsorption capacity at different pH values; (e) violet color changes with time for Cr (VI) adsorbed by M3.

**Table 1.** The Cr (VI) concentration of samples deduced for 20 min.

	pH	Adsorption Percentage	Adsorption Capacity (mg/g)	Fe: Ni (Weight)
NZVI	5.6	5.42%	22.56	\
MWCNTs	5.6	4.80%	19.95	\
M1	5.6	32.35%	134.57	\
M2	5.6	52.07%	216.60	2:1
M3	5.6	53.95%	224.43	5:1
M4	5.6	40.95%	170.37	10:1
M5	5.6	35.22%	146.50	1:1
M6	5.6	39.88%	165.89	20:1
M7	5.6	52.52%	218.46	3:1
M3R	5.6	49.38%	205.41	5:1

The adsorption capacities of M3 that has been recycled were examined 1–5 times. As shown in Figure 7a, in the Cr (VI) removal test for M3 with 1–5 replicates, the adsorption capacities are 205.41 mg/g, 204.91 mg/g, 204.48 mg/g, 204.55 mg/g, and 203.80 mg/g.

Figure 7b shows the violet color of Cr (VI) adsorbed by recycled M3 for comparison. More than 90% of M3's adsorption capacity is retained after five cycles of recycling, while there is no discernible decrease with increasing cycles. These data indicate that M3 is highly recyclable. In the initial synthesis of M3, iron ions were precipitation-adsorbed to the surface of the MWCNTs from liquid, resulting in nanoparticles with a smaller particle size and better dispersion. However, during the reprocessing of M3, the iron nanoparticles were converted from a trivalent solid precipitation, resulting in a larger average particle size and poorer dispersion. The different nanoparticle formation processes explain the small decrease in the adsorption capacity of M3 during the first reuse. Subsequent iterations showed little continued reduction in adsorption capacity, as the treatment process was identical.

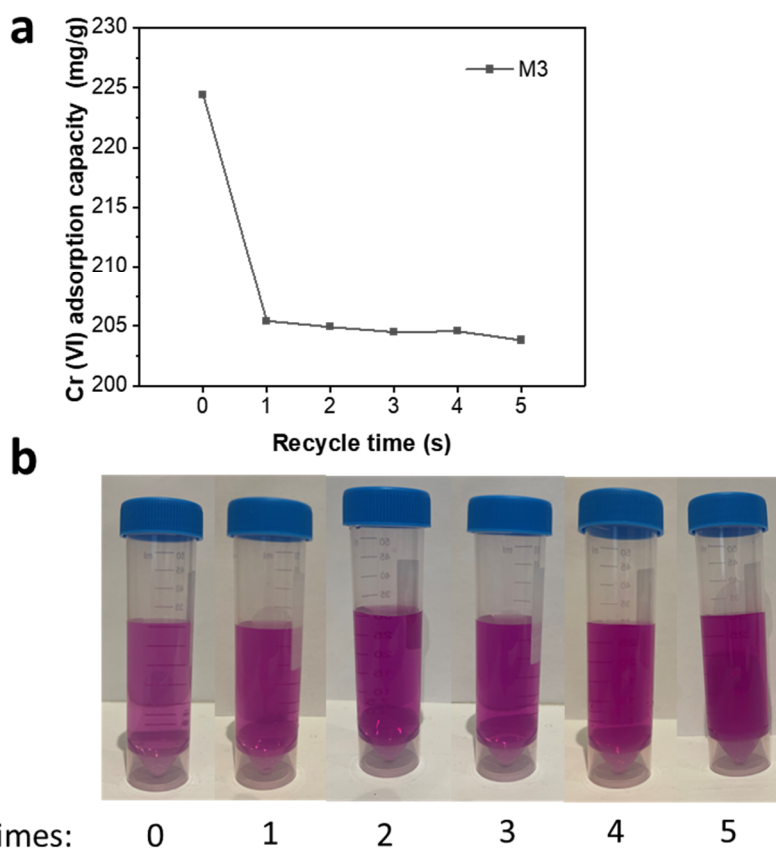


**Figure 7.** (a) Cr (VI) adsorption capacities for M3 with 1–5 replicates; (b) images of the violet color for Cr (VI) adsorbed by recycled M3.

The pH of the solution plays an important role in Cr (VI) adsorption. In order to determine how pH affects Cr (VI) adsorption, Cr (VI) adsorption experiments were conducted at pH = 4.8, 5.6, and 6.4. As shown in Table A2, the Cr (VI) adsorption capacity decreased as pH increased, which is consistent with previous research [67]. The highest adsorption capacity was observed for M3 at pH = 4.8 for 256.87 mg/g.

Furthermore, to verify the stability of samples, samples were left to stand in the solution for 3 months after the Cr (VI) adsorption experiment, and the Cr (VI) concentration in solution was characterized. The results are presented in Table A3. All samples remained stable and retained more than 93% of their adsorption capacity. This is because the Cr (III) hydroxide produced is stable and difficult to disperse back into the solution once it has been adsorbed by Fe–Ni/MWCNTs.

A comparison of Cr (VI) adsorption capacity with the reported MWCNTs or CNTs-related materials is shown in Table A4. As discussed previously, a higher pH has a negative impact on adsorption capacity; compared with the listed literature, this study demonstrates a significantly higher adsorption capacity for Cr (VI) even under negative pH effects.



Under similar conditions, Fe–Ni/MWCNTs had a 20% higher Cr (VI) adsorption capacity than Fe–Ni/RGO.

As shown in Figure 6c, the adsorption kinetics of Cr (VI) are obtained by determining the adsorption capacity of samples at different times. Initially, adsorption is rapid due to the enormous number of available sites, but it slows down with time and reaches equilibrium after 20 min. The results are analyzed using pseudo-first-order kinetic models and pseudo-second-order kinetic models. This pseudo-first-order kinetic model can be expressed linearly as follows:

$$\log(q_e - q_t) = \log q_e - K_1 t$$

The pseudo-second-order kinetic model can be expressed in linear form as follows:

$$\frac{t}{q_t} = \frac{1}{K_2 q_e^2} + \frac{t}{q_e}$$

where  $q_e$  and  $q_t$  (mg/g) represent Cr (VI) adsorption capacity at equilibrium and  $t$  time (hour).  $K_1$  (g/mg/min) and  $K_2$  (g/mg/min) represent the pseudo-first-order kinetic model and pseudo-second-order kinetic model rate constants, respectively. The results of the analysis for the pseudo-first-order kinetic model and the pseudo-second-order kinetic model are displayed in Table 2. As compared with the pseudo-first-order kinetic model, the pseudo-second-order kinetic model obtained an adjusted  $R^2$  that is closer to 1, which indicates that the pseudo-second-order kinetic model is more appropriate for the samples. In this study, it is confirmed that the adsorption process is not physical but chemical in nature.

**Table 2.** Pseudo-first-order kinetic model and pseudo-second-order kinetic model results.

	M1	M3	M3R
	Pseudo-first-order kinetic model		
$q_e$ (mg/g)	149.9628	221.5793	203.0504
$K_1$ (g/mg/min)	0.1252	0.1755	0.1719
$R^2$ -adjusted	0.9860	0.9904	0.9855
	Pseudo-second-order kinetic model		
$q_e$ (mg/g)	169.6151	249.8790	229.4719
$K_2$ (g/mg/min)	0.0020	0.0023	0.0024
$R^2$ -adjusted	0.9316	0.9766	0.9801

#### 2.4. Cr (VI) Reduce Reaction Mechanism and Kinetic Model

In this nano-composite, in combination with the dispersant, the spatial barrier effect of MWCNTs reduces the agglomeration of Fe–Ni bimetallic particles. It functions as an adsorbent to enrich the Cr (VI) surrounding the material, which increases the directionality of the chemical reduction capacity of the material and also provides part of the Cr (VI) adsorption capacity based on its own physical adsorption. Fe functions as a reducing agent to convert Cr (VI) to Cr (III), which is less susceptible to re-oxidation in nature, preventing secondary contamination. In the reduction process, Cr (VI) reacts with Fe (0) to form Cr (OH)<sub>3</sub> and Fe (OH)<sub>3</sub> precipitates. The added nickel has a higher reduction potential than Fe, which promotes the electron transfer of Fe (0) as the anode through electrochemical coupling, which enhances the reduction activity of iron nanoparticles; furthermore, the nickel nanopowder is also able to catalyse the hydrogenolysis reaction and improve the hydrogenation reaction of nano iron. These hydroxides precipitate and encapsulate Fe (0), preventing all iron from participating in the reaction, which is slowed down by the physical adsorption ability of the MWCNTs to adsorb some of the hydroxide precipitates onto its surface. The process is schematically illustrated in Figure 8.

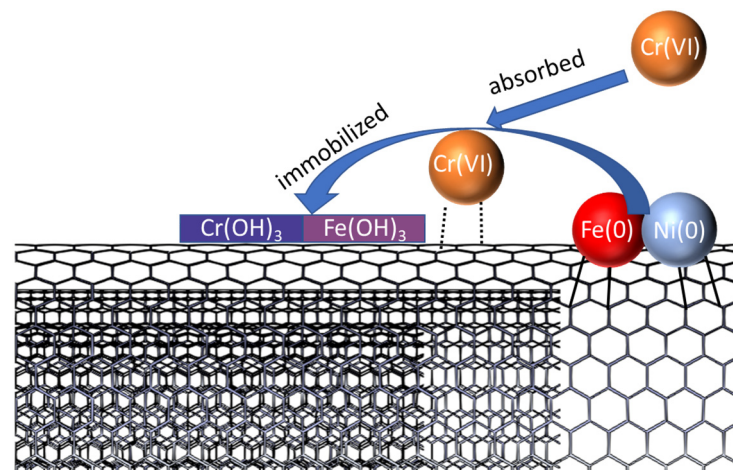
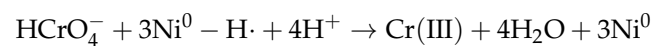
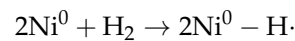
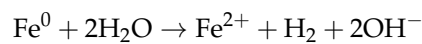
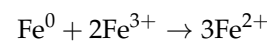
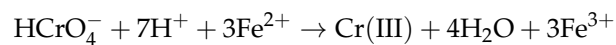
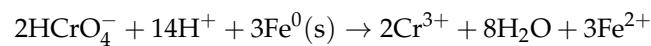


**Figure 8.** Cr (VI) adsorption and reduction mechanism of samples.

All the formulae of the chemical reactions occurring in the Cr removal experiments are listed below:



The major Cr (VI) status at a low pH is  $\text{HCrO}_4^-$  and  $\text{Cr}_2\text{O}_7^{2-}$  [68]. The removal efficiency is greater at low pH values due to the highly protonated and positively charged surface of the adsorbent. Electrostatic force can attract  $\text{HCrO}_4^-$  and  $\text{Cr}_2\text{O}_7^{2-}$  to the adsorbent. As the pH increases, the reaction rate and equilibrium are significantly affected by less  $\text{H}^+$  and more  $\text{OH}^-$ . In addition, the surface of the adsorbent will be negatively charged, which drastically reduces its adsorption capacity.

As Cr (VI) adsorption is not a pure chemical or physical reaction, traditional pseudo-first-order kinetic models and pseudo-second-order kinetics cannot adequately describe it. All electrons are transferred from Fe species to Cr species; Fe is the only element capable of reducing Cr (VI). The rate equation for the Cr (VI) reduction is based on the concentration of Cr (VI) and the samples. The conversion ratio between Cr (VI) and Cr (III) is 1:1. A kinetic model can be applied [49]. The equation can be expressed as follows:

$$[\text{Cr(VI)}]_t = \frac{[\text{Cr(VI)}]_0 \{C_{\text{SC}}^*[\text{S}] - [\text{Cr(VI)}]_0\}}{C_{\text{SC}}^*[\text{S}] \exp\{k(C_{\text{SC}}^*[\text{S}] - [\text{Cr(VI)}]_0 t)\} - [\text{Cr(VI)}]_0}$$

where  $[\text{Cr(VI)}]$  represents the hexavalent chromium concentration (mmol/L) at time  $t$ ;  $k$  represents rate coefficient ( $\text{L mmol}^{-1} \text{min}^{-1}$ );  $C_{\text{SC}}^*[\text{S}]$ , represents the initial concentration of  $[\text{SC}]$ ;  $[\text{S}]$  represents the sample concentration (g/L);  $C_{\text{SC}}^*$  represents the removal capacity of Cr (VI) per unit gram of sample (mmol/g);  $k$  and  $C_{\text{SC}}^*$  are the model constant parameters; and  $t$  represents the reaction time (s). The fit result of the kinetic model is shown in Figure 9 and Table 3. The kinetic model exhibits a high adjusted  $R^2$ , which confirms that the reaction mechanism and model are reasonable for the reduction reaction. By comparing the rate coefficient  $k$  between M1 and M3, it is determined that Ni (0) added to M3 increased the reaction coefficient by a considerable amount, which is the result of Ni's catalyst effect. In

the meantime, comparing M3 and M3R, the decrease in  $K$  and  $C_{SC}^*$  is due to the aggregation of Fe (0) and Ni (0) during the second reduction of Fe–Ni/MWCNTs.

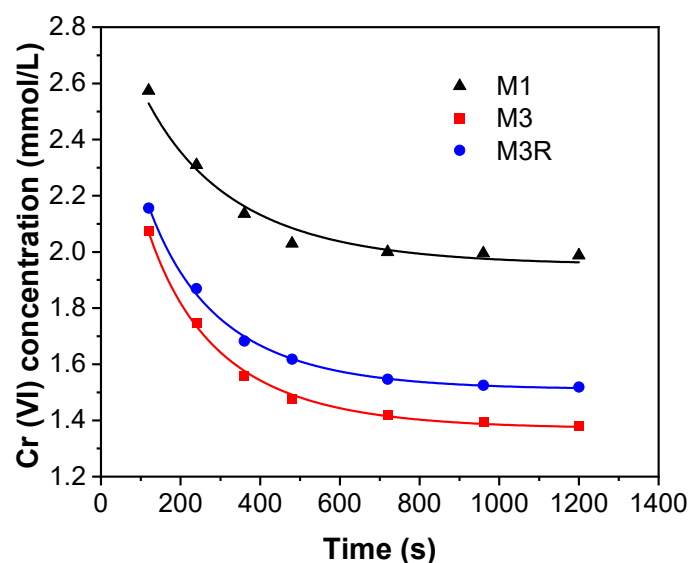


Figure 9. The kinetic model curve for M1, M3, and M3R.

Table 3. The kinetic model results.

	M1	M3	M3R
$K$ (L mmol <sup>-1</sup> min <sup>-1</sup> )	0.0178	0.1734	0.1650
$C_{SC}^*$ (mmol/g)	2.8162	4.3445	3.9733
R2-adjusted	0.9981	0.9974	0.9972

### 3. Materials and Methods

#### 3.1. Materials and Instruments

##### 3.1.1. Materials

MWCNTs and nickel (II) chloride hexahydrate were supplied by Sigma-Aldrich (Dorset, UK). FeCl<sub>3</sub>·6H<sub>2</sub>O and potassium dichromate (K<sub>2</sub>Cr<sub>4</sub>O<sub>7</sub>) were supplied by SLS (Scientific Laboratory Supplies). Polyvinyl pyrrolidone (PVP) and chromium (III) chloride hexahydrate (CrCl<sub>3</sub>) were purchased from Alfa Aesar. Sodium borohydride (NaBH<sub>4</sub>) was supplied by Fisher Scientific Ltd., and 1,5-diphenylcarbazide (DPC) was purchased from Sigma-Aldrich. The chemicals were used as received without further purification.

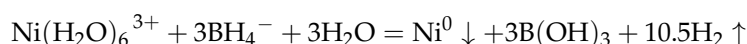
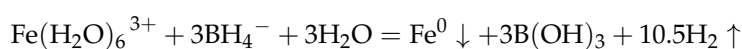
##### 3.1.2. Instruments

A scanning electron microscope (SEM, SU8230, Hitachi, Tokyo, Japan) equipped for energy-dispersive X-ray spectroscopy (EDS) was used to characterize the morphology, bonding patterns, and elemental distribution of the various components in a multi-component material, respectively. A transmission electron microscope (TEM, FEI Tecnai TF20) was used to observe the morphological changes in the components of the material before and after Cr (VI) removal tests to help analyse the reaction mechanism. Fourier-transform infrared spectroscopy (FTIR) experiments were performed with a Thermo Scientific Nicolet iS10 FTIR Spectrometer (Thermo Scientific, Waltham, MA, USA) to characterize the type and content of residual oxygen-containing groups on MWCNTs. BET surface areas were tested on a Tristar 3000 (Micromeritics) to analyze the effect of different components on the specific surface area and pore size distribution of the material. Ultraviolet-visible spectroscopy (UV-Vis) spectra of samples were measured by a UV spectrophotometer UV-1800 (Shimadzu, Kyoto, Japan) to quantify the concentration of Cr (VI) in each solution. Sample size characterization was investigated by dynamic light scattering (DLS) measurements

using the Zetasizer Nano ZS (Malvern Panalytical, Malvern, UK). This was used to analyse the loading and agglomeration of metal particles. HAXPES UHV-XPS (X-ray photoelectron spectroscopy) was used to confirm the existence and the valence states of elements before and after the Cr (VI) removal experiment.

### 3.2. Preparation of Fe/MWCNTs and Fe–Ni/MWCNTs Composites

The FeCl<sub>3</sub> solution was formed by adding different amounts of 30 wt% FeCl<sub>3</sub>·6H<sub>2</sub>O solution to 50 mL of deionized water under magnetic stirring for 30 min, and then 0.32 g MWCNTs, 2.0 g PVP, and a certain amount of NiCl<sub>2</sub>·6H<sub>2</sub>O were added in sequence and magnetically stirred overnight. In different samples, Fe–Ni ratios were adjusted, but the total mass of Fe and Ni elements remained the same at 0.2 g. Afterwards, 40 mL of 50 mg/mL NaBH<sub>4</sub> was added dropwise to the system and stirred overnight. As a reducing agent, NaBH<sub>4</sub> reduced Fe (III) and Ni (II) to Fe (0) and Ni (0) NPs, respectively. During this period, mechanical oscillation replaced magnetic stirring in order to prevent Fe (0) NPs from being affected by the magnetic field. The production of H<sub>2</sub> during this step requires careful control. Here are the reaction equations:



Following vacuum filtration, the final product was washed three times with ethanol, dried overnight in a vacuum oven, and then collected and stored with nitrogen protection. For the purpose of comparison, seven samples were prepared as shown in Table 4.

**Table 4.** Detailed reaction conditions of different samples.

Sample	60 wt% FeCl <sub>3</sub> Solution (mL)	MWCNTs (g)	NiCl <sub>2</sub> ·6H <sub>2</sub> O (g)	PVP (g)	NaBH <sub>4</sub> (g)	Fe: Ni (Weight)
M1	1.033	0.320	\	2	2	\
M2	1.278	0.320	0.534	2	2	2:1
M3	1.606	0.320	0.268	2	2	5:1
M4	1.760	0.320	0.156	2	2	10:1
M5	0.968	0.320	0.808	2	2	1:1
M6	1.839	0.320	0.078	2	2	20:1
M7	1.452	0.320	0.404	2	2	3:1

After the Cr (VI) adsorption capacity experiment of M3, the sediment was collected by vacuum filtration. The collected sediment was named M3A. Then, half of the M3A was dispersed in 25 mL DI water containing 1.0 g PVP under mechanical oscillation overnight. Afterwards, excess NaBH<sub>4</sub> solution was added dropwise with mechanical oscillation. Then, the sediment was collected by vacuum filtration, washed with ethanol three times, and dried in vacuum oven overnight. The collected dried sediment was named M3R.

### 3.3. Cr (VI) Adsorption Capacity Test

The Cr (VI) adsorption capacity of samples was measured by the DPC method. In an acidic environment, DPC combines with Cr (VI) ions to produce a violet solution with a characteristic peak at max = 545 nm [69]. Prior to measurement, buffers with pH values 4.8, 5.6, and 6.2 were prepared using phosphoric acid (H<sub>3</sub>PO<sub>4</sub>) and sodium hydroxide solution (NaOH). An amount of 15 mg of each sample was added to 34 mL of pH buffer (pH = 5.6), followed by ultrasonic dispersion to ensure that the sample was fully dispersed. Afterwards, 6 mL of 20 mmol/L Cr (VI) solution was added to the solution to form a solution of Cr (VI) at a concentration of 3 mmol/L. The solution remained mechanically oscillated. At the scheduled time, 0.5 mL of solution was drawn and added to a bottle containing 2 mL of DPC solution and 22.5 mL of water. After 5 min, the UV absorption spectrum was measured to determine the amount of Cr (VI) remaining in the solution.

#### 4. Conclusions

In this research, a novel Cr (VI) removal material was designed and produced comprising multi-walled carbon nanotubes (MWCNTs) as a support with a high specific surface area and Fe–Ni bimetallic particles as a catalyst loaded onto MWCNTs through the coprecipitation and physisorption method. Such a design produced composites with properties of high adsorption, reduction, and immobilisation of Cr (VI) for removal. Furthermore, they can be easily recollected and reused. The results indicate that the added Ni nearly tripled the BET surface area compared with samples without Ni, and added Ni increased the Cr (VI) adsorption capacity significantly. Fe–Ni/MWCNTs composites exhibited the highest Cr (VI) adsorption capacity of 224.43 mg/g at pH = 5.6 and 256.87 mg/g at pH = 4.8, which are about twice those values reported for other materials under similar conditions. At least 93% of the adsorption capacity remained for reused samples, which demonstrates a good reusability. With a low cost of the raw materials, facile synthesis process, and good reusability, Fe–Ni/MWCNTs show great potential for future industrialisation.

**Author Contributions:** Conceptualization, Z.K. and D.W.; data curation, Z.K. and H.G.; formal analysis, Z.K. and H.G.; funding acquisition, D.W.; investigation, Z.K.; methodology, Z.K., H.G. and D.W.; project administration, X.J. and D.W.; resources, Z.K., X.M. and D.W.; supervision, X.J. and D.W.; validation, Z.K., H.G. and X.M.; visualization, Z.K. and H.G.; writing—original draft, Z.K.; writing—review and editing, Z.K., H.G. and D.W. All authors have read and agreed to the published version of the manuscript.

**Funding:** This study was funded by the University of Leeds and Beihang University.

**Institutional Review Board Statement:** Not applicable.

**Informed Consent Statement:** Not applicable.

**Data Availability Statement:** Not applicable.

**Conflicts of Interest:** The authors declare no conflict of interest.

**Sample Availability:** Samples of the compounds Fe–Ni/MWCNTs are available from the authors.

#### Appendix A

Peak 2 has a smaller diameter than M3 for M3A. This is due to Fe (0) being consumed by Cr (VI) during the reduction process of Cr (VI). In addition, Peak 2 intensity for M3A increased from 6.9% for M3 to 32.4%. This is indicative of Fe–Ni bimetal falling off the surface of MWCNTs following Cr (VI) reduction. As can be seen from Table A1, Peak 2 for M3R is larger than Peak 2 for M3 and M3A. As a result, Fe–Ni nanoparticles agglomerate during the second reduction of Fe–Ni/MWCNTs. It is anticipated that the agglomeration of Fe–Ni nano iron will negatively affect the adsorption capacity of Cr (VI). The intensity of Peak 2 for M3R decreased from 32.4% to 16.9%, indicating that part of the Fe–Ni bimetal that was lost in M3A was decorated back on the surface of MWCNTs during the second reduction of Fe–Ni/MWCNTs. The reusability of samples can be enhanced by this method.

**Table A1.** Size distribution determined by the intensity.

	Peak 1		Peak 2	
	Size (d. nm)	% Intensity	Size (d. nm)	% Intensity
M1	684.3	79.1	54.85	20.9
M2	555.0	90.7	66.46	9.3
M3	461.5	93.1	64.91	6.9
M4	544.2	86.6	46.01	13.4
M5	261.5	92.6	51.31	7.4
M6	919.7	91.2	55.24	8.8
M7	605.1	92.0	78.95	8.0
M3R	370.0	83.1	96.96	16.9
M3A	519.5	67.6	48.06	32.4

**Table A2.** pH effects on Cr (VI) adsorption.

	Adsorption Percentage			Adsorption Capacity (mg/g)		
	pH = 5.6	pH = 4.8	pH = 6.4	pH = 5.6	pH = 4.8	pH = 6.4
M1	32.35%	38.00%	29.38%	134.57	158.06	122.24
M2	52.07%	40.91%	30.74%	216.60	245.87	197.40
M3	53.95%	59.10%	47.45%	224.43	256.87	207.09
M4	40.95%	61.75%	49.78%	170.37	197.77	150.42
M5	35.22%	47.54%	36.16%	146.50	175.77	133.45
M6	39.88%	42.25%	32.08%	165.89	203.18	148.18
M7	52.52%	48.84%	35.62%	218.46	246.61	201.50

**Table A3.** Sample stability for Cr (VI) adsorption.

	pH	Adsorption Percentage	Adsorption Capacity (mg/g)	After 3 Months	Adsorption Capacity Left
M1	5.6	32.35%	134.57	131.03	97.37%
M2	5.6	52.07%	216.60	205.97	95.09%
M3	5.6	53.95%	224.43	217.16	96.76%
M4	5.6	40.95%	170.37	164.59	96.61%
M5	5.6	35.22%	146.50	141.84	96.82%
M6	5.6	39.88%	165.89	155.83	93.93%
M7	5.6	52.52%	218.46	212.68	97.35%

**Table A4.** Cr (VI) adsorption capacity reported in the literature.

Raw Material	pH	Adsorption Capacity (mg/g)	References
CNTs supported by activated carbon	2.0	9.0	[70]
ionic liquid functionalized oxidized MWCNTs	2.8	85.83	[42]
MWCNTs-COOH-immobilized HSO <sub>4</sub>	2.0	31.29	[71]
Magnetic iron oxide MWCNTs	3.0	12.61	[72]
FeMnO <sub>x</sub> decorated MWCNTs	2.0	47.25	[73]
α-Fe <sub>2</sub> O <sub>3</sub> /MWCNTs	6.0	Around 75	[74]
ZnO-functionalized MWCNTs	2.0	Up to 140	[75]
Fe-Ni/RGO	6.0	176.74	[49]
Fe-Ni/RGO	5.0	197.43	[49]
Fe-Ni/MWCNTs	4.8	256.87	This work
Fe-Ni/MWCNTs	5.6	224.43	This work
Fe-Ni/MWCNTs	6.4	207.09	This work

## References

- Miensah, E.; Khan, M.M.; Chen, J.Y.; Zhang, X.M.; Wang, P.; Zhang, Z.X.; Jiao, Y.; Liu, Y.; Yang, Y. Zeolitic imidazolate frameworks and their derived materials for sequestration of radionuclides in the environment: A review. *Crit. Rev. Environ. Sci. Technol.* **2020**, *50*, 1874–1934. [CrossRef]
- Varela, J.P.; Valente, A.J.M.; Durães, L. Assessment of heavy metal pollution from anthropogenic activities and remediation strategies: A review. *J. Environ. Manag.* **2019**, *246*, 101–118. [CrossRef] [PubMed]
- Tang, J.; Zhang, J.; Ren, L.; Zhou, Y.; Gao, J.; Luo, L.; Yang, Y.; Peng, Q.; Huang, H.; Chen, A. Diagnosis of soil contamination using microbiological indices: A review on heavy metal pollution. *J. Environ. Manag.* **2019**, *242*, 121–130. [CrossRef] [PubMed]
- He, J.; Yang, Y.; Christakos, G.; Liu, Y.; Yang, X. Assessment of soil heavy metal pollution using stochastic site indicators. *Geoderma* **2019**, *337*, 359–367. [CrossRef]
- Shen, H.; Chen, J.; Dai, H.; Wang, L.; Hu, M.; Xia, Q. New Insights into the Sorption and Detoxification of Chromium(VI) by Tetraethylenepentamine Functionalized Nanosized Magnetic Polymer Adsorbents: Mechanism and pH Effect. *Ind. Eng. Chem. Res.* **2013**, *52*, 12723–12732. [CrossRef]
- Mortvedt, J.J. Heavy Metal Contaminants in Inorganic and Organic Fertilizers. In *Fertilizers and Environment: Proceedings of the International Symposium "Fertilizers and Environment", Salamanca, Spain, 26–29 September 1994*; Springer: Dordrecht, The Netherlands, 1996; pp. 5–11. [CrossRef]

7. Zhao, Y.; Zhao, D.; Chen, C.; Wang, X. Enhanced photo-reduction and removal of Cr(VI) on reduced graphene oxide decorated with TiO<sub>2</sub> nanoparticles. *J. Colloid Interface Sci.* **2013**, *405*, 211–217. [[CrossRef](#)]
8. Verma, R.; Dwivedi, P. Heavy metal water pollution-A case study. *Recent Res. Sci. Technol.* **2013**, *5*, 98–99.
9. Islam, M.; Mohana, A.A.; Rahman, A.; Rahman, M.; Naidu, R.; Rahman, M.M. A Comprehensive Review of the Current Progress of Chromium Removal Methods from Aqueous Solution. *Toxics* **2023**, *11*, 252. [[CrossRef](#)]
10. Duan, C.; Ma, T.; Wang, J.; Zhou, Y. Removal of heavy metals from aqueous solution using carbon-based adsorbents: A review. *J. Water Process. Eng.* **2020**, *37*, 101339. [[CrossRef](#)]
11. Adam, M.R.; Salleh, N.M.; Othman, M.H.D.; Matsuura, T.; Ali, M.H.; Puteh, M.H.; Ismail, A.; Rahman, M.A.; Jaafar, J. The adsorptive removal of chromium (VI) in aqueous solution by novel natural zeolite based hollow fibre ceramic membrane. *J. Environ. Manag.* **2018**, *224*, 252–262. [[CrossRef](#)]
12. Gottipati, R.; Mishra, S. Preparation of microporous activated carbon from Aegle Marmelos fruit shell and its application in removal of chromium(VI) from aqueous phase. *J. Ind. Eng. Chem.* **2016**, *36*, 355–363. [[CrossRef](#)]
13. Rahman, A.; Lamb, D.; Rahman, M.M.; Bahar, M.; Sanderson, P.; Abbasi, S.; Bari, A.F.; Naidu, R. Removal of arsenate from contaminated waters by novel zirconium and zirconium-iron modified biochar. *J. Hazard. Mater.* **2021**, *409*, 124488. [[CrossRef](#)] [[PubMed](#)]
14. Ku, Y.; Jung, I.-L. Photocatalytic reduction of Cr(VI) in aqueous solutions by UV irradiation with the presence of titanium dioxide. *Water Res.* **2000**, *35*, 135–142. [[CrossRef](#)] [[PubMed](#)]
15. Gould, J. The kinetics of hexavalent chromium reduction by metallic iron. *Water Res.* **1982**, *16*, 871–877. [[CrossRef](#)]
16. Blowes, D.; Ptacek, C. Geochemical remediation of groundwater by permeable reactive walls: Removal of chromate by reaction with iron-bearing solids. In Proceedings of the Subsurface Restoration Conference, 3rd International Conference on Ground Water Quality Research, Dallas, TX, USA, 21–24 June 1992.
17. Chang, L.-Y. Alternative chromium reduction and heavy metal precipitation methods for industrial wastewater. *Environ. Prog.* **2003**, *22*, 174–182. [[CrossRef](#)]
18. Blowes, D.W.; Ptacek, C.J.; Jambor, J.L. In-Situ Remediation of Cr(VI)-Contaminated Groundwater Using Permeable Reactive Walls: Laboratory Studies. *Environ. Sci. Technol.* **1997**, *31*, 3348–3357. [[CrossRef](#)]
19. Cao, J.; Zhang, W.-X. Stabilization of chromium ore processing residue (COPR) with nanoscale iron particles. *J. Hazard. Mater.* **2006**, *132*, 213–219. [[CrossRef](#)]
20. Ramos, M.A.V.; Yan, W.; Li, X.-Q.; Koel, B.E.; Zhang, W.-X. Simultaneous Oxidation and Reduction of Arsenic by Zero-Valent Iron Nanoparticles: Understanding the Significance of the Core–Shell Structure. *J. Phys. Chem. C* **2009**, *113*, 14591–14594. [[CrossRef](#)]
21. Boparai, H.K.; Joseph, M.; O'carroll, D.M. Kinetics and thermodynamics of cadmium ion removal by adsorption onto nano zerovalent iron particles. *J. Hazard. Mater.* **2011**, *186*, 458–465. [[CrossRef](#)]
22. Hwang, Y.-H.; Kim, D.-G.; Shin, H.-S. Mechanism study of nitrate reduction by nano zero valent iron. *J. Hazard. Mater.* **2011**, *185*, 1513–1521. [[CrossRef](#)]
23. Lv, Z.; Yang, S.; Chen, L.; Alsaedi, A.; Hayat, T.; Chen, C. Nanoscale zero-valent iron/magnetite carbon composites for highly efficient immobilization of U(VI). *J. Environ. Sci.* **2019**, *76*, 377–387. [[CrossRef](#)] [[PubMed](#)]
24. Li, S.; Wang, W.; Liang, F.; Zhang, W.-X. Heavy metal removal using nanoscale zero-valent iron (nZVI): Theory and application. *J. Hazard. Mater.* **2017**, *322*, 163–171. [[CrossRef](#)]
25. O'carroll, D.; Sleep, B.; Krol, M.; Boparai, H.; Kocur, C. Nanoscale zero valent iron and bimetallic particles for contaminated site remediation. *Adv. Water Resour.* **2013**, *51*, 104–122. [[CrossRef](#)]
26. Yu, S.; Pang, H.; Huang, S.; Tang, H.; Wang, S.; Qiu, M.; Chen, Z.; Yang, H.; Song, G.; Fu, D.; et al. Recent advances in metal-organic framework membranes for water treatment: A review. *Sci. Total Environ.* **2021**, *800*, 149662. [[CrossRef](#)] [[PubMed](#)]
27. Kocur, C.M.; Sleep, B.E.; O'carroll, D.M. Moving into the Third Decade of Nanoscale Zero-Valent Iron (NZVI) Development: Best Practices for Field Implementation. In *Nanoscale Zerovalent Iron Particles for Environmental Restoration*; Springer: Cham, Switzerland, 2019; pp. 293–333. [[CrossRef](#)]
28. Quiton, K.G.N.; Lu, M.-C.; Huang, Y.-H. Synthesis and catalytic utilization of bimetallic systems for wastewater remediation: A review. *Chemosphere* **2021**, *262*, 128371. [[CrossRef](#)] [[PubMed](#)]
29. Wang, S.; Zhao, M.; Zhou, M.; Li, Y.C.; Wang, J.; Gao, B.; Sato, S.; Feng, K.; Yin, W.; Igalavithana, A.D.; et al. Biochar-supported nZVI (nZVI/BC) for contaminant removal from soil and water: A critical review. *J. Hazard. Mater.* **2019**, *373*, 820–834. [[CrossRef](#)] [[PubMed](#)]
30. Huang, Q.; Liu, W.; Peng, P.; Huang, W. Reductive dechlorination of tetrachlorobisphenol A by Pd/Fe bimetallic catalysts. *J. Hazard. Mater.* **2013**, *262*, 634–641. [[CrossRef](#)]
31. Lai, B.; Zhang, Y.; Chen, Z.; Yang, P.; Zhou, Y.; Wang, J. Removal of p-nitrophenol (PNP) in aqueous solution by the micron-scale iron–copper (Fe/Cu) bimetallic particles. *Appl. Catal. B Environ.* **2014**, *144*, 816–830. [[CrossRef](#)]
32. Angaru, G.K.R.; Choi, Y.-L.; Lingamdinne, L.P.; Choi, J.-S.; Kim, D.-S.; Koduru, J.R.; Yang, J.-K.; Chang, Y.-Y. Facile synthesis of economical feasible fly ash–based zeolite–supported nano zerovalent iron and nickel bimetallic composite for the potential removal of heavy metals from industrial effluents. *Chemosphere* **2021**, *267*, 128889. [[CrossRef](#)]
33. Wen, Z.; Lu, J.; Zhang, Y.; Cheng, G.; Huang, S.; Chen, J.; Xu, R.; Ming, Y.-A.; Wang, Y.; Chen, R. Facile inverse micelle fabrication of magnetic ordered mesoporous iron cerium bimetal oxides with excellent performance for arsenic removal from water. *J. Hazard. Mater.* **2020**, *383*, 121172. [[CrossRef](#)]

34. Huang, S.; Ouyang, T.; Chen, J.; Wang, Z.; Liao, S.; Li, X.; Liu, Z.-Q. Synthesis of nickel–iron layered double hydroxide via topochemical approach: Enhanced surface charge density for rapid hexavalent chromium removal. *J. Colloid Interface Sci.* **2022**, *605*, 602–612. [[CrossRef](#)] [[PubMed](#)]
35. Li, S.; Cai, M.; Liu, Y.; Wang, C.; Yan, R.; Chen, X. Constructing Cd<sub>0.5</sub>Zn<sub>0.5</sub>S/Bi<sub>2</sub>WO<sub>6</sub> S-scheme heterojunction for boosted photocatalytic antibiotic oxidation and Cr(VI) reduction. *Adv. Powder Mater.* **2023**, *2*, 100073. [[CrossRef](#)]
36. Wen, Z.; Zhang, Y.; Guo, S.; Chen, R. Facile template-free fabrication of iron manganese bimetal oxides nanospheres with excellent capability for heavy metals removal. *J. Colloid Interface Sci.* **2017**, *486*, 211–218. [[CrossRef](#)]
37. Liu, W.-J.; Qian, T.-T.; Jiang, H. Bimetallic Fe nanoparticles: Recent advances in synthesis and application in catalytic elimination of environmental pollutants. *Chem. Eng. J.* **2014**, *236*, 448–463. [[CrossRef](#)]
38. Borah, B.J.; Saikia, H.; Bharali, P. Reductive conversion of Cr(vi) to Cr(iii) over bimetallic CuNi nanocrystals at room temperature. *New J. Chem.* **2014**, *38*, 2748–2751. [[CrossRef](#)]
39. Mokete, R.; Eljamal, O.; Sugihara, Y. Exploration of the reactivity of nanoscale zero-valent iron (NZVI) associated nanoparticles in diverse experimental conditions. *Chem. Eng. Process. Intensif.* **2020**, *150*, 107879. [[CrossRef](#)]
40. Jinhua, W.; Xiang, Z.; Bing, Z.; Yafei, Z.; Rui, Z.; Jindun, L.; Rongfeng, C. Rapid adsorption of Cr (VI) on modified halloysite nanotubes. *Desalination* **2010**, *259*, 22–28. [[CrossRef](#)]
41. Shaheen, S.M.; Niazi, N.K.; Hassan, N.E.E.; Bibi, I.; Wang, H.; Tsang, D.C.W.; Ok, Y.S.; Bolan, N.; Rinklebe, J. Wood-based biochar for the removal of potentially toxic elements in water and wastewater: A critical review. *Int. Mater. Rev.* **2019**, *64*, 216–247. [[CrossRef](#)]
42. Krishna Kumar, A.S.; Jiang, S.-J.; Tseng, W.-L. Effective adsorption of chromium(vi)/Cr(iii) from aqueous solution using ionic liquid functionalized multiwalled carbon nanotubes as a super sorbent. *J. Mater. Chem. A* **2015**, *3*, 7044–7057. [[CrossRef](#)]
43. Zhou, H.; Ma, M.; Zhao, Y.; Baig, S.A.; Hu, S.; Ye, M.; Wang, J. Integrated green complexing agent and biochar modified nano zero-valent iron for hexavalent chromium removal: A characterisation and performance study. *Sci. Total Environ.* **2022**, *834*, 155080. [[CrossRef](#)]
44. Bharath, G.; Rambabu, K.; Banat, F.; Hai, A.; Arangadi, A.F.; Ponpandian, N. Enhanced electrochemical performances of peanut shell derived activated carbon and its Fe<sub>3</sub>O<sub>4</sub> nanocomposites for capacitive deionization of Cr(VI) ions. *Sci. Total Environ.* **2019**, *691*, 713–726. [[CrossRef](#)] [[PubMed](#)]
45. Yang, W.; Xi, D.; Li, C.; Yang, Z.; Lin, Z.; Si, M. “In-situ synthesized” iron-based bimetal promotes efficient removal of Cr(VI) in by zero-valent iron-loaded hydroxyapatite. *J. Hazard. Mater.* **2021**, *420*, 126540. [[CrossRef](#)] [[PubMed](#)]
46. Lu, H.; Tian, B.; Wang, J.; Hao, H. Montmorillonite-Supported Fe/Ni Bimetallic Nanoparticles for Removal of Cr (VI) from Wastewater. *Chem. Eng. Trans.* **2017**, *60*, 169–174.
47. Zeng, S.; Zhong, D.; Xu, Y.; Zhong, N. Biochar-loaded nZVI/Ni bimetallic particles for hexavalent chromium removal from aqueous solution. *J. Dispers. Sci. Technol.* **2022**, 1–12. [[CrossRef](#)]
48. Bharath, G.; Hai, A.; Kiruthiga, T.; Rambabu, K.; Sabri, M.A.; Park, J.; Choi, M.Y.; Banat, F.; Haija, M.A. Fabrication of Ru–CoFe<sub>2</sub>O<sub>4</sub>/RGO hierarchical nanostructures for high-performance photoelectrodes to reduce hazards Cr(VI) into Cr(III) coupled with anodic oxidation of phenols. *Chemosphere* **2022**, *299*, 134439. [[CrossRef](#)]
49. Kang, Z.; Gao, H.; Hu, Z.; Jia, X.; Wen, D. Ni–Fe/Reduced Graphene Oxide Nanocomposites for Hexavalent Chromium Reduction in an Aqueous Environment. *ACS Omega* **2022**, *7*, 4041–4051. [[CrossRef](#)]
50. Arunkumar, T.; Karthikeyan, R.; Subramani, R.R.; Viswanathan, K.; Anish, M. Synthesis and characterisation of multi-walled carbon nanotubes (MWCNTs). *Int. J. Ambient. Energy* **2020**, *41*, 452–456. [[CrossRef](#)]
51. Nie, P.; Min, C.; Song, H.-J.; Chen, X.; Zhang, Z.; Zhao, K. Preparation and Tribological Properties of Polyimide/Carboxyl-Functionalized Multi-walled Carbon Nanotube Nanocomposite Films Under Seawater Lubrication. *Tribol. Lett.* **2015**, *58*, 1–12. [[CrossRef](#)]
52. Li, J.; Lu, G.; Wu, G.; Mao, D.; Guo, Y.; Wang, Y.; Guo, Y. The role of iron oxide in the highly effective Fe-modified Co<sub>3</sub>O<sub>4</sub> catalyst for low-temperature CO oxidation. *RSC Adv.* **2013**, *3*, 12409–12416. [[CrossRef](#)]
53. Mikhaylov, V. Optical and thermal properties of sol–gel Al(OH)<sub>3</sub>–Fe(OH)<sub>3</sub>–PVA composite films. *J. Sol-Gel Sci. Technol.* **2019**, *92*, 282–292. [[CrossRef](#)]
54. Pan, C.; Liu, H.; Catalano, J.G.; Wang, Z.; Qian, A.; Giammar, D.E. Understanding the Roles of Dissolution and Diffusion in Cr(OH)<sub>3</sub> Oxidation by δ-MnO<sub>2</sub>. *ACS Earth Space Chem.* **2019**, *3*, 357–365. [[CrossRef](#)]
55. Amonette, J.E.; Rai, D. Identification of Noncrystalline (Fe,Cr)(OH)<sub>3</sub> by Infrared Spectroscopy. *Clays Clay Miner.* **1990**, *38*, 129–136. [[CrossRef](#)]
56. Papassiopi, N.; Vaxevanidou, K.; Christou, C.; Karagianni, E.; Antipas, G. Synthesis, characterization and stability of Cr(III) and Fe(III) hydroxides. *J. Hazard. Mater.* **2014**, *264*, 490–497. [[CrossRef](#)] [[PubMed](#)]
57. Kalidhasan, S.; KrishnaKumar, A.S.; Rajesh, V.; Rajesh, N. Ultrasound-assisted preparation and characterization of crystalline cellulose–ionic liquid blend polymeric material: A prelude to the study of its application toward the effective adsorption of chromium. *J. Colloid Interface Sci.* **2012**, *367*, 398–408. [[CrossRef](#)]
58. Kalidhasan, S.; Kumar, A.S.K.; Rajesh, V.; Rajesh, N. Enhanced adsorption of hexavalent chromium arising out of an admirable interaction between a synthetic polymer and an ionic liquid. *Chem. Eng. J.* **2013**, *222*, 454–463. [[CrossRef](#)]
59. Kumar, R.; Kamakshi; Kumar, M.; Awasthi, K. Functionalized Pd-decorated and aligned MWCNTs in polycarbonate as a selective membrane for hydrogen separation. *Int. J. Hydrogen Energy* **2016**, *41*, 23057–23066. [[CrossRef](#)]



60. Arputharaj, E.; Kumar, A.S.K.; Tseng, W.-L.; Jiang, S.-J.; Huang, Y.-L.; Dahms, H.-U. Self-Assembly of Poly(ethyleneimine)-Modified g-C<sub>3</sub>N<sub>4</sub> Nanosheets with Lysozyme Fibrils for Chromium Detoxification. *Langmuir* **2021**, *37*, 7147–7155. [[CrossRef](#)]
61. Chen, X.; Wang, X.; Zhang, X.; Srinivas, K.; Liu, D.; Zhao, X.; Yu, H.; Wang, B.; Zhang, W.; Chen, Y. Vertical Fe(OH)<sub>3</sub>/Ni<sub>9</sub>S<sub>8</sub> nanoarrays electrodeposited on stainless steel as binder-free electrocatalyst for highly efficient and stable oxygen evolution reaction. *J. Mater. Sci.* **2021**, *56*, 19144–19154. [[CrossRef](#)]
62. Akia, M.; Mkhoyan, K.A.; Lozano, K. Synthesis of multiwall  $\alpha$ -Fe<sub>2</sub>O<sub>3</sub> hollow fibers via a centrifugal spinning technique. *Mater. Sci. Eng. C* **2019**, *102*, 552–557. [[CrossRef](#)]
63. Chen, H.; Fan, Y.; Fan, Z.; Xu, H.; Cui, D.; Xue, C.; Zhang, W. Noble-metal-free p-n heterojunction of iron(III) hydroxide and graphitic carbon nitride for hydrogen evolution reaction. *Ceram. Int.* **2021**, *47*, 35057–35066. [[CrossRef](#)]
64. Yamashita, T.; Hayes, P. Analysis of XPS spectra of Fe<sup>2+</sup> and Fe<sup>3+</sup> ions in oxide materials. *Appl. Surf. Sci.* **2008**, *254*, 2441–2449. [[CrossRef](#)]
65. Bahgat, M.; Farghali, A.A.; El Roubi, W.M.; Khedr, M.H. Efficiency, Kinetics and Thermodynamics of Toluidine Blue Dye Removal from Aqueous Solution Using MWCNTs Decorated with NiFe<sub>2</sub>O<sub>4</sub>. *Fullerenes* **2014**, *22*, 454–470. [[CrossRef](#)]
66. Xiao, C.; Leng, X.; Zhang, X.; Zheng, K.; Tian, X. Improved thermal properties by controlling selective distribution of AlN and MWCNT in immiscible polycarbonate (PC)/Polyamide 66 (PA66) composites. *Compos. Part A Appl. Sci. Manuf.* **2018**, *110*, 133–141. [[CrossRef](#)]
67. Liu, W.; Jin, L.; Xu, J.; Liu, J.; Li, Y.; Zhou, P.; Wang, C.; Dahlgren, R.A.; Wang, X. Insight into pH dependent Cr(VI) removal with magnetic Fe<sub>3</sub>S<sub>4</sub>. *Chem. Eng. J.* **2019**, *359*, 564–571. [[CrossRef](#)]
68. García-Sosa, I.; Olguín, M.T. Comparison between the Cr(VI) adsorption by hydrotalcite and hydrotalcite-gibbsite compounds. *Sep. Sci. Technol.* **2015**, *50*, 2631–2638. [[CrossRef](#)]
69. Liao, J.; Wu, Y.; Chen, X.; Yu, H.; Lin, Y.; Huang, K.; Zhang, J.; Zheng, C. Light-triggered oxidative activity of chromate at neutral pH: A colorimetric system for accurate and on-site detection of Cr(VI) in natural water. *J. Hazard. Mater.* **2022**, *440*. [[CrossRef](#)]
70. Atieh, M.A. Removal of Chromium (VI) from polluted water using carbon nanotubes supported with activated carbon. *Procedia Environ. Sci.* **2011**, *4*, 281–293. [[CrossRef](#)]
71. Sun, L.; Wang, M.; Li, W.; Luo, S.; Wu, Y.; Ma, C.; Liu, S. Adsorption Separation of Cr(VI) from a Water Phase Using Multiwalled Carbon Nanotube-Immobilized Ionic Liquids. *ACS Omega* **2020**, *5*, 22827–22839. [[CrossRef](#)]
72. Lee, C.; Kim, S. Cr(VI) Adsorption to Magnetic Iron Oxide Nanoparticle-Multi-Walled Carbon Nanotube Adsorbents. *Water Environ. Res.* **2016**, *88*, 2111–2120. [[CrossRef](#)]
73. Ma, T.; Wu, Y.; Liu, N.; Yan, C. Adsorption behavior of Cr(VI) and As(III) on multiwall carbon nanotubes modified by iron-manganese binary oxide (FeMnO<sub>x</sub>/MWCNTs) from aqueous solution. *Sep. Sci. Technol.* **2022**, *57*, 192–208. [[CrossRef](#)]
74. Verdugo, E.M.; Xie, Y.; Baltrusaitis, J.; Cwiertny, D.M. Hematite decorated multi-walled carbon nanotubes ( $\alpha$ -Fe<sub>2</sub>O<sub>3</sub>/MWCNTs) as sorbents for Cu(II) and Cr(VI): Comparison of hybrid sorbent performance to its nanomaterial building blocks. *RSC Adv.* **2016**, *6*, 99997–100007. [[CrossRef](#)]
75. Murali, A.; Sarswat, P.K.; Free, M.L. Adsorption-coupled reduction mechanism in ZnO-Functionalized MWCNTs nanocomposite for Cr(VI) removal and improved anti-photocorrosion for photocatalytic reduction. *J. Alloys Compd.* **2020**, *843*, 155835. [[CrossRef](#)]

**Disclaimer/Publisher's Note:** The statements, opinions and data contained in all publications are solely those of the individual author(s) and contributor(s) and not of MDPI and/or the editor(s). MDPI and/or the editor(s) disclaim responsibility for any injury to people or property resulting from any ideas, methods, instructions or products referred to in the content.